UC Santa Cruz
UC Santa Cruz Previously Published Works

Title
Highly Tunable Hollow Gold Nanospheres: Gaining Size Control and Uniform Galvanic Exchange of Sacrificial Cobalt Boride Scaffolds

Permalink
https://escholarship.org/uc/item/5tg3c9j1

Journal
ACS Applied Materials & Interfaces, 10(15)

ISSN
1944-8244

Authors
Lindley, Sarah A
Cooper, Jason K
Rojas-Andrade, Mauricio D
et al.

Publication Date
2018-04-18

DOI
10.1021/acsami.8b00726

Supplemental Material
https://escholarship.org/uc/item/5tg3c9j1#supplemental

Peer reviewed

eScholarship.org Powered by the California Digital Library
University of California

ACS APPLIED MATERIALS & INTERFACES

Research Article

Cite This: ACS Appl. Mater. Interfaces XXXX, XXX, XXX−XXX

www.acsami.org

Highly Tunable Hollow Gold Nanospheres: Gaining Size Control and Uniform Galvanic Exchange of Sacrificial Cobalt Boride Scaffolds

Sarah A. Lindley,[†] Jason K. Cooper,[‡] Mauricio D. Rojas-Andrade,[†] Victoria Fung,[†] Conor J. Leahy,[†] Shaowei Chen,[†] and Jin Z. Zhang*,[†]

[†]Department of Chemistry and Biochemistry, University of California, Santa Cruz, California 95064, United States

[‡]Chemical Sciences Division, Joint Center for Artificial Photosynthesis, Lawrence Berkeley National Laboratory, Berkeley, California 94720, United States

Supporting Information

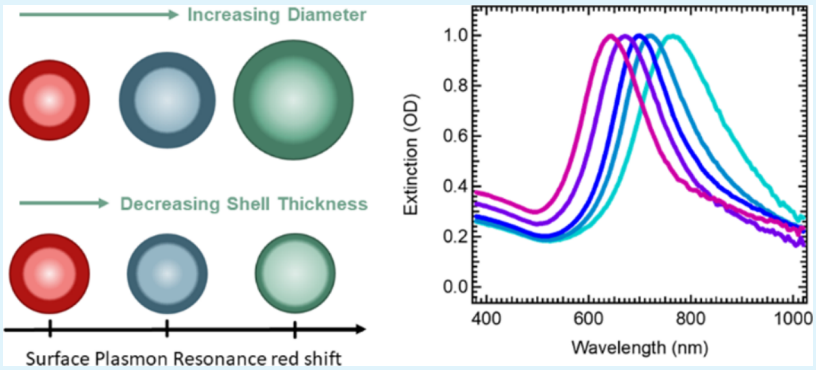

ABSTRACT: In principle, the diameter and surface plasmon resonance (SPR) frequency of hollow metal nanostructures can be independently adjusted, allowing the formation of targeted photoactivated structures of specific size and optical functionality. Although tunable SPRs have been reported for various systems, the shift in SPR is usually concomitant with a change in particle size. As such, more advanced tunability, including constant diameter with varying SPR or constant SPR with varying diameter, has not been properly achieved experimentally. Herein, we demonstrate this advanced tunability with hollow gold nanospheres (HGNs). HGNs were synthesized through galvanic exchange using cobalt-based nanoparticles (NPs) as sacrificial scaffolds. Co_2B NP scaffolds were prepared by sodium borohydride nucleation of aqueous cobalt chloride and characterized using UV−vis, dynamic light scattering, X-ray absorption spectroscopy, and X-ray photoelectron spectroscopy. Careful control over the size of the Co_2B scaffold and its galvanic conversion is essential to realize fine control of the resultant HGN diameter and shell thickness. In pursuit of size control, we introduce $B(OH)_4^-$ (the final product of $NaBH_4$ hydrolysis) as a growth agent to obtain hydrodynamic diameters ranging from ∼17−85 nm with relative standard deviation <3%. The highly monodisperse Co_2B NPs were then used as scaffolds for the formation of HGNs. In controlling HGN shell thickness and uniformity, environmental oxygen was shown to affect both the structural and optical properties of the resultant gold shells. With careful control of these key factors, we demonstrate an HGN synthesis that enables independent variation of diameter and shell thickness, and thereby SPR, with unprecedented uniformity. The new synthesis method creates a truly tunable plasmonic nanostructure platform highly desirable for a wide range of applications, including sensing, catalysis, and photothermal therapy.

KEYWORDS: *cobalt boride, size control, sodium borohydride, galvanic exchange, hollow gold nanospheres, surface plasmon resonance*

INTRODUCTION

Plasmonic metal nanostructures exhibit beneficial optical properties owing to their surface plasmon resonance (SPR), the collective oscillation of conduction band electrons that manifests as strong absorption, and/or scattering at the oscillation frequency.[1,2] As oscillation frequency is structure dependent, the SPR may be tuned by changing the size or shape of the nanoparticle (NP).[3−5] This tunability positions plasmonic metal NPs as highly attractive components in nanomedicine,[6−12] optoelectronics,[13−18] sensing,[6−9,13,18,19] and solar energy conversion.[20−24] In these applications, hollow metal nanostructures have distinct advantages over their solid metal counterparts including lower mass per particle for reduced material costs, higher surface-area-to-volume ratio for increased density of loading or catalytic sites, and enhanced plasmonic performance in applications like surface-enhanced Raman scattering (SERS), drug delivery, and catalysis.[25−30] Furthermore, the SPR of hollow structures are more tunable as the hollow core provides an additional parameter by which to modify the overall electronic structure. For one hollow

Received: January 14, 2018
Accepted: March 2, 2018

© XXXX American Chemical Society

DOI: 10.1021/acsami.8b00726
ACS Appl. Mater. Interfaces XXXX, XXX, XXX−XXX

structure of note, the hollow gold nanosphere (HGN), the SPR may be tuned across the visible wavelengths and into the near-infrared by adjusting the ratio of outer diameter to shell thickness (the aspect ratio).[31] Increasing the aspect ratio and red-shifting the SPR may be accomplished by either increasing the diameter or thinning the shell. Because of this twofold tunability, the diameter and SPR frequency can in principle be independently adjusted, allowing the formation of targeted photoactivated structures of specific size and optical functionality. As such, HGNs could therefore become a powerful platform for a variety of nano-enabled applications.

Since the introduction of HGNs in 2005, much work has been done to elucidate their structure-dependent optical properties,[31−35] gain reproducibility of synthesis,[36,37] and demonstrate their use in a variety of applications.[38−41] However, their formation mechanism has not yet been controlled to the point of achieving independent selection of both size and SPR. To this end, the synthesis must be investigated and improved to enable a high degree of control over diameter and shell thickness.

HGN diameters are determined by those of their cobalt-based NP scaffolds, sacrificial templates onto which shells of gold are formed through galvanic exchange (GE).[31,42] These scaffolds are commonly made through sodium borohydride nucleation of aqueous cobalt salt. Although this reaction is often studied, it is not yet well understood. Disagreement exists in the literature over the identity of the main product (e.g., various cobalt−boron alloys have been reported), and size control methods remain elusive. In 2006, Schwartzberg et al. reported that small adjustments in overall scaffold diameter may be made by changes to the volume of both the sodium borohydride reducing agent and sodium citrate capping ligand used in scaffold synthesis, but larger sizes proved difficult to achieve reproducibly.[31] In 2009, a combination of alcohol solvents and a triblock copolymer surfactant were used to synthesize Co_2B NPs ranging from 3.2 to 171.4 nm in diameter, but the larger size regime was plagued by broad size dispersion and precipitation, and analysis of the mid-range size regime reveals large relative standard deviation (RSD).[43] In 2011, silica-coated Co−B NPs were synthesized from 50 to 250 nm in diameter with improved RSD by adjusting the ratio of surfactant to cobalt salt precursor, but silica coating was required for particle stability and small size regimes were not demonstrated.[44] Recently, Pu et al. showed that reaction temperature may be used to slow nucleation and promote growth from 24 to 122 nm in diameter but some resultant particles were polydisperse and exact sizes were difficult to achieve reproducibly.[45] Although progress has been made, size control methods for cobalt-based NP systems remain limited and fine adjustments over a large size range have not been realized experimentally.

For a given scaffold diameter, the SPR frequency and full width at half-maximum of the resultant HGNs are determined by their shell thickness and uniformity, structural parameters that are governed by the GE process. Previously, Schwartzberg et al. showed that shell thickness could be increased simply by providing more gold during GE[31] but other factors affecting shell structure and uniformity have not been explored. One such factor is environmental oxygen. GE in HGN synthesis has traditionally been performed under aerobic conditions[31−37,39−42,45] with cobalt as a starting template because of its favorable reduction potential and ease of oxidation in air.[46−49] This ease of oxidation allows facile removal of residual core material after shell formation without relying on post-processing techniques like wet-chemical etching. However, competition between GE with gold and direct oxidation of the scaffold in air can potentially disrupt the reduction of gold and thus the shell uniformity.

In this work, we first investigate the formation of Co_2B NP scaffolds made from sodium borohydride nucleation of aqueous cobalt chloride. In pursuit of size control, we introduce $B(OH)_4^-$ (the final product of BH_4^- hydrolysis) as a growth agent, capable of slowing the nucleation of cobalt ions and promoting coalescence, thereby increasing the final size of the particles. Using this new protocol, we demonstrate the synthesis of highly monodisperse scaffolds, achieving incremental increases in hydrodynamic diameter over a ∼17−85 nm range. To our knowledge, this is the first demonstration of fine control of Co_2B NP diameter while maintaining monodispersity. Second, in pursuit of shell control, we investigate the role of environmental oxygen in the GE process. Finally, combining insights from all results, we demonstrate a well-controlled synthesis of HGNs, enabling the formation of high quality monodisperse HGNs with twofold tunability over a range of selected diameter and SPR combinations.

■ METHODS AND EXPERIMENTAL SECTION

Synthesis of Co_2B NP Scaffolds. Cobalt(II) chloride hexahydrate ($CoCl_2·6H_2O$) was purchased from Sigma-Aldrich, trisodium citrate dihydrate ($Na_3C_6H_5O_7·2H_2O$) was purchased from VWR International, and sodium borohydride ($NaBH_4$) was purchased from Fisher Scientific. All water used in synthesis was ultrapure in quality, with a resistivity of 18.3 MΩ.

Co_2B NP scaffolds were synthesized via the well-established nucleation of Co^{2+} ions with $NaBH_4$, using citrate as a capping ligand. Briefly, a 100 mL solution of 0.40 mM $CoCl_2·6H_2O$ and 4.0 mM $Na_3C_6H_5O_7·2H_2O$ was prepared in a 500 mL round-bottom flask and deaerated by bubbling with nitrogen for 1 h. During this time, the solution was stirred at 700 rpm with a magnetic stir bar. Then, a given volume of freshly prepared aqueous 1 M $NaBH_4$ (25−200 μL) was injected while the solution continued to stir under nitrogen protection. After the addition of $NaBH_4$, the solution turned from pale pink to brown, indicating the reduction of Co^{2+} ions and the formation of the Co_2B NP scaffold. After 2 min, the stir bar was magnetically suspended above the solution and the Co_2B NPs were subsequently allowed to stand under a constant nitrogen flow for 2 h to ensure complete hydrolysis of the borohydride nucleation agent.

Control of the Co_2B NP Diameter. To synthesize larger Co_2B NPs, a given volume of $B(OH)_4^-$ (20−200 μL) was added to the freshly prepared aqueous 1 M $NaBH_4$ and quickly mixed before being injected into the cobalt salt solution. The presence of $B(OH)_4^-$ prolonged the onset of color change from pale pink to brown/gray. To obtain $B(OH)_4^-$, a 1.0 mL aliquot of aqueous 1.0 M $NaBH_4$ was prepared and allowed to hydrolyze under ambient conditions for 48 h.

Co K-Edge XANES. The Co K-edge X-ray absorption near edge structure (XANES) spectra were collected at the Stanford Synchrotron Radiation Lightsource (SSRL) on beamline 7−3 with an average current of 300 mA at an electron energy of 3.0 GeV. The radiation was monochromatized using a Si(220) double crystal monochromator, which was detuned to 50% of its maximum at the Co K-edge. The intensity of the incident X-rays (I_0) was monitored by an N_2-filled ion chamber in front of the sample. The monochromator energy was calibrated by using the first peak maximum of the first derivative of the Co foil spectrum (7709.5 eV). The solution-based samples were collected using a sealed glass cell with a silicon nitride window covering a hole in the glass cell through which the X-rays were incident into the solution. The sample was placed in an N_2-purged box fitted with Kapton tape windows. The sample fluorescence signal was recorded using a 30-element Ge detector (Canberra) with the samples at 45° to the incident beam. Co K-edge data were collected for

DOI: 10.1021/acsami.8b00726
ACS Appl. Mater. Interfaces XXXX, XXX, XXX−XXX

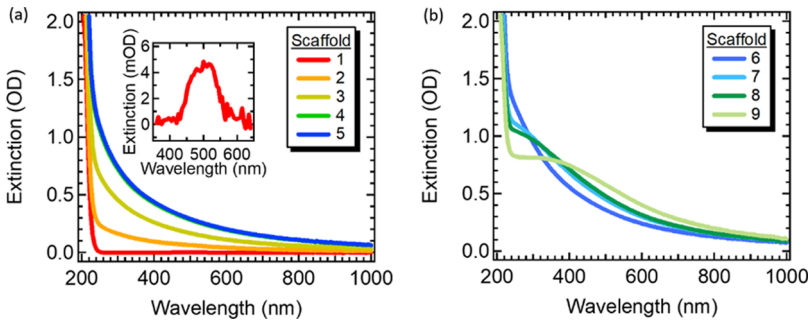

Figure 1. (a) Extinction spectra of Co_2B NPs made with BH_4^-/Co^{2+} molar ratios ranging from 0 to 5.00 (scaffolds 1−5). With no reducing agent, scaffold 1 represents only aqueous citrate and $CoCl_2$. As such, an absorption feature for hydrated Co^{2+} ions can be seen at 500 nm, as highlighted in the inset. (b) Co_2B NP extinction for scaffolds made with $B(OH)_4^-/BH_4^-$ ratios of 0.500, 1.00, and 2.00 (scaffolds 6−9). Associated synthetic parameters are reported in Table 1.

solutions of 0.4 M $CoCl_2$ and 0.4 M $CoCl_2$ + 0.8 M $NaBH_4$. A powdered reference sample of commercially available $Co(OH)_2$ was collected without further purification by dilution in boron nitride (∼1% w/w) and then packed into 0.5 mm-thick aluminum sample holders using Kapton film windows on both sides. Data reduction of the XAS spectra was performed using SamView (SixPACK software, Samuel M. Webb, SSRL). Athena software (IFEFFIT package) was used to subtract the pre-edge and postedge contributions, and the results were normalized with respect to the edge jump.

X-ray Photoelectron Spectroscopy. X-ray photoelectron spectroscopy (XPS) was performed using a monochromatized Al Kα source ($h\nu$ = 1486.6 eV), operated at 225 W, on a Kratos Axis Ultra DLD system at a takeoff angle of 0° relative to the surface normal, and pass energy for narrow scan core level and valence band spectra of 20 eV. A tungsten filament charge neutralizer was utilized for the powdered samples. Spectral fitting was done using CasaXPS analysis software. Spectral positions were corrected using adventitious carbon by shifting the C 1s core-level position to 284.8 eV, and curves were fitted with quasi-Voigt lines following Shirley background subtraction. The samples were prepared in a nitrogen glove box.

UV−Visible Spectroscopy. UV−vis spectra were recorded with an Agilent Technologies Cary 60 UV−vis spectrophotometer using a 700 μL quartz cuvette with 10 mm optical path length. For Co_2B NP extinction measurement, 500 μL aliquots were extracted from the solutions under nitrogen protection and immediately transferred to the spectrophotometer.

Dynamic Light Scattering. Dynamic light scattering (DLS) was performed on a DynaPro NanoStar from Wyatt Technology using Dynamics software version 7.1.7. The data acquisition parameters included water solvent, spherical radius of gyration (R_g) model, temperature of 20.000 °C, and 30 acquisitions. The reported ± values represent one standard deviation from the mean. RSD represents one standard deviation as a percentage of the mean, using unrounded values for calculation. For the measurement, 200 μL aliquots were extracted from the solutions under nitrogen protection and immediately transferred to the DLS instrument.

Cyclic Voltammetry. Cyclic voltammograms (CVs) of $NaBH_4$ were taken on a Pine potentiostat (model AFCBP1) using an Au wire working electrode, a Pt coil counter electrode, and an Hg/HgO (1.0 M KOH) reference electrode. To hydrolyze the sample, 1.0 mL of 1.0 M aqueous $NaBH_4$ was prepared and left sitting under ambient conditions. At each time point, a 100 μL aliquot was transferred to 9.90 mL of 0.10 M KOH to suppress continued hydrolysis during measurement. CVs were taken at three time points (0, 24, and 48 h) using a 2.500 V/s sweep rate.

^{11}B NMR. Proton-coupled ^{11}B NMR was performed on a Bruker 500 MHz NMR using 5 mm-thin-walled Quartz NMR tubes (Wilmad, 528-PP-7QTZ) to eliminate extraneous boron signal. At each time point, an 80 μL aliquot of the 1.0 M aqueous $NaBH_4$ was transferred to 720 μL of 0.10 M KOH to create a 0.10 M $NaBH_4$ solution. A 720 μL aliquot of this solution was added to 80 μL D_2O to make a final 10% v/v deuterated solution for frequency locking.

Synthesis of Hollow Gold Nanospheres. Chloroauric acid ($HAuCl_4$) was purchased from Fisher Scientific. All water used in synthesis was ultrapure in quality, with a resistivity of 18.3 MΩ. For anaerobic GE, a given volume (1.00−10.0 μL) of 0.10 M $HAuCl_4$ was added to 15 mL of ultrapure water and deaerated by bubbling with nitrogen gas for 1 h under magnetic stirring at 700 rpm. Once deaerated, GE was initiated by transferring 15 mL of the Co_2B NP solution to the stirring gold solution via air-free cannula transfer. The resultant Co_2B NP/Au core/shell particles were stirred for 2 min under nitrogen protection at 700 rpm before final oxidation of the remaining Co_2B NP cores. The residual cobalt cores were fully oxidized either by removing the septa and stirring at 700 rpm for 3 min under ambient conditions or by transferring a 3.0 mL aliquot to a vial and vortexing for 10 s. For aerobic GE, a given volume (1.00−10.0 μL) of 0.10 M $HAuCl_4$ was added to 15 mL of ultrapure water and stirred for 60 min (to be consistent with the anaerobic protocol) under ambient conditions. GE was initiated by transferring 15 mL of the Co_2B NP solution to the stirring gold solution via cannula transfer in air. The resultant Co_2B NP/Au core/shell particles were stirred for 5 min at 700 rpm under ambient conditions to ensure complete oxidation of the residual Co_2B NP cores.

Electron Microscopy. Scanning electron microscopy (SEM) was performed at the W.M. Keck Center for Optofluidics at the University of California, Santa Cruz on an FEI Quanta 3D field emission microscope operated at 5.00 kV acceleration voltage. Because the Co_2B NP scaffolds are air-sensitive, great care was taken in preparing them for SEM. The as-formed Co_2B NP scaffolds, synthesized under nitrogen protection, were transferred into an air-free glove box where they were centrifuged at 5000 rpm for 15 min. After removing the supernatant, the concentrated solution was dropped onto a hexagonal, 400 mesh copper grid with a carbon support film of standard 5−6 nm thickness (Electron Microscopy Sciences) and allowed to dry in the glove box under vacuum and nitrogen protection. When dry, the grid was immediately transferred to the microscope. HGN solutions were centrifuged twice under ambient conditions at 13 000 rpm for 2 min and resuspended in ultrapure water. High-resolution transmission electron microscopy (HRTEM) was performed at the National Center for Electron Microscopy (NCEM) at the Lawrence Berkeley National Laboratory Molecular Foundry on an FEI UT Tecnai microscope operated at 200 kV acceleration voltage. Diameter measurements were taken directly from HRTEM images using ImageJ software. For each sample, at least 50 HGN diameters were used to calculate the average diameter ± one standard deviation. Additionally, 12 shell thickness measurements were taken for each HGN measured. Individual HGNs were matched with their associated shell thickness measurements to determine the aspect ratio.

RESULTS AND DISCUSSION

Optical and Structural Characterization of Co_2B NP Scaffolds Made with BH_4^- Reducing Agent. Co_2B NPs were synthesized through the well-established reaction between

DOI: 10.1021/acsami.8b00726
ACS Appl. Mater. Interfaces XXXX, XXX, XXX−XXX

aqueous cobalt chloride and sodium borohydride in the presence of a citrate capping ligand.[31,42] Although the NPs produced by this method have often been described as elemental cobalt, various cobalt borides have been experimentally identified as the main products.[50−52] In agreement with these reports, in situ XANES spectra collected at the Co K-edge before and after the addition of borohydride confirm that Co^0 is not produced in our system. XPS spectra collected on the isolated brown cobalt-based product confirm the lack of metallic character. Taken together, these results are in better agreement with what has been reported in the literature for Co_2B, as detailed in Supporting Information Discussion S1. A commonly accepted reaction mechanism with Co_2B as the final product is shown in eq 1.[50]

$$2CoCl_2 + 4NaBH_4 + 9H_2O \rightarrow Co_2B + 4NaCl + 12.5H_2 + 3B(OH)_3 \quad (1)$$

To control the size of NPs, an understanding of their nucleation and growth processes is essential. In classical nucleation theory as set forth by LaMer in the 1950s, particle diameter is said to be governed by the extent of initial nucleation.[53,54] To investigate the effect of initial nucleation on the final Co_2B NP diameter, Co_2B NP syntheses were carried out with BH_4^-/Co^{2+} molar ratios ranging from 0 to 5.00. According to eq 1, 2 mol of BH_4^- are needed to reduce every 1 mol of Co^{2+}. Thus, only BH_4^-/Co^{2+} ratios greater than 2.00 will provide BH_4^- in excess of what is required for the full reduction of cobalt ions.

The resultant scaffolds were characterized by their extinction spectra, as shown in Figure 1a. In the absence of a reducing agent, the extinction spectrum consisted only of a large signal at ultraviolet (UV) wavelengths representing the presence of citrate and a small peak ∼500 nm representing the $^4T_{1g}(f) \rightarrow {}^4T_{1g}(p)$ d electron transition of hydrated Co^{2+} ions (red curve).[55] When reducing agent was provided, the cobalt solution turned from pale pink to brown and the extinction spectrum gained low signal throughout the visible range, indicating the formation of Co_2B NPs (scaffold 2−5). The increasing extent of nucleation with increasing BH_4^-/Co^{2+} ratio is apparent by the gradual increase of the Co_2B-related extinction. Saturation is observed between 1.25 and 2.50 BH_4^-/Co^{2+}, consistent with eq 1. Resultant hydrodynamic diameters were then assessed with DLS, as tabulated in Table 1. Importantly, the hydrodynamic diameters of all Co_2B NPs agree to within one standard deviation. Because the reaction between BH_4^- and $CoCl_2$ is fast, nucleation occurs rapidly but growth cannot proceed because of the lack of additional reactant after the initial injection. Thus, simply increasing or decreasing the amount of sodium borohydride may affect the extent of nucleation but is not enough to appreciably control the size of the resultant NPs for this system.

Table 1. Synthetic Parameters and Resultant Hydrodynamic Diameter (Mean ± One Standard Deviation) for Co_2B NP Scaffolds

scaffold	BH_4^-/Co^{2+}	$B(OH)_4^-/BH_4^-$	hydrodynamic diameter (nm)
1	0	0	NA
2	0.625	0	19 ± 3
3	1.25	0	21 ± 2
4	2.50	0	19 ± 2
5	5.00	0	23 ± 3
6	5.00	0.500	43 ± 2
7	5.00	1.00	56 ± 1
8	2.50	1.00	61 ± 1
9	2.50	2.00	76 ± 2

Many recent studies on the formation mechanism of colloidal metal NPs from wet-chemical reduction of metal salt precursors have reported mechanisms that deviate from classical nucleation theory.[56−62] For instance, for the reduction of $HAuCl_4$ with $NaBH_4$, a two-step mechanism has been described: metal ions are swiftly reduced to small clusters, which then rapidly coalesce to form the final particles. A similar mechanism was reported for the reduction of $AgClO_4$ with $NaBH_4$, and it was found that clusters aggregate and coalesce until reaching a size at which there is sufficient stability to halt the process. In both reports, the extent of aggregation and coalescence, as opposed to the extent of initial nucleation, was determined to be the controlling factor in final NP size. Interestingly, in the case of $AgClO_4$ reduction, the onset of aggregation and coalescence was shown to arise from a destabilization of colloidal stability correlated with the hydrolysis of excess BH_4^- to $B(OH)_4^-$. By contrast, for our cobalt system, the conversion of residual BH_4^- to $B(OH)_4^-$ does not promote additional coalescence; the resultant scaffold size is the same whether BH_4^- is in excess or not. However, the presence of $B(OH)_4^-$ during initial nucleation may indeed affect the formation of Co_2B NPs. It has been recently shown that the decomposition of sodium borohydride during storage leads to significant changes in the resulting Co_2B particles.[63] As $B(OH)_4^-$ is the final decomposition product, we investigated its role in Co_2B formation and its effect on the final particle diameter.

Optical and Structural Characterization of Co_2B NP Scaffolds Made with $B(OH)_4^-$ Growth Agent. To investigate the potential effect of $B(OH)_4^-$ on Co_2B NP formation, syntheses were repeated with $B(OH)_4^-$ provided alongside the BH_4^- reducing agent. To obtain $B(OH)_4^-$, aqueous 1.0 M $NaBH_4$ was hydrolyzed for 48 h. The product was characterized and identified with proton-coupled ^{11}B NMR and cyclic voltammetry, as detailed in Supporting Information Discussion S2. Table 1 displays the DLS results for Co_2B NPs made with $B(OH)_4^-/BH_4^-$ molar ratios ranging from 0.500 to 2.00 and a molar excess of BH_4 (scaffolds 6−9). In all cases, the addition of $B(OH)_4^-$ during the initial nucleation of cobalt ions resulted in an increase in scaffold diameter. In fact, the resultant scaffold is largest for large $B(OH)_4/BH_4^-$ ratios and small BH_4^-/Co^{2+} ratios (scaffold 9). Importantly, the extinction spectrum can be used as an indicator of scaffold size. The extinction spectra for ∼20 nm scaffolds followed a normal exponential decay (Figure 1a) but an inflection was apparent at ∼240 nm for that of the 43 ± 2 nm scaffold (Figure 1b, scaffold 6). In the case of larger sizes, the inflection grew into a small extinction feature that broadened and red-shifted with increasing diameter (Figure 1b, scaffolds 7−9). To our knowledge, this is the first experimental evidence of a size-dependent extinction feature in Co_2B NPs.

Elucidating the Role of $B(OH)_4^-$ in the Co_2B NP Growth Mechanism. To better understand the role of $B(OH)_4^-$ as a growth agent, Co_2B NP formation was investigated by time-resolved UV−vis for scaffolds 5 and 7. These scaffolds were made with an equivalent amount of BH_4^- (5.00 BH_4^-/Co^{2+}) but varying amounts of $B(OH)_4^-$ (0 and 1.00 $B(OH)_4^-/BH_4^-$, respectively). Three-dimensional extinc-

DOI: 10.1021/acsami.8b00726
ACS Appl. Mater. Interfaces XXXX, XXX, XXX−XXX

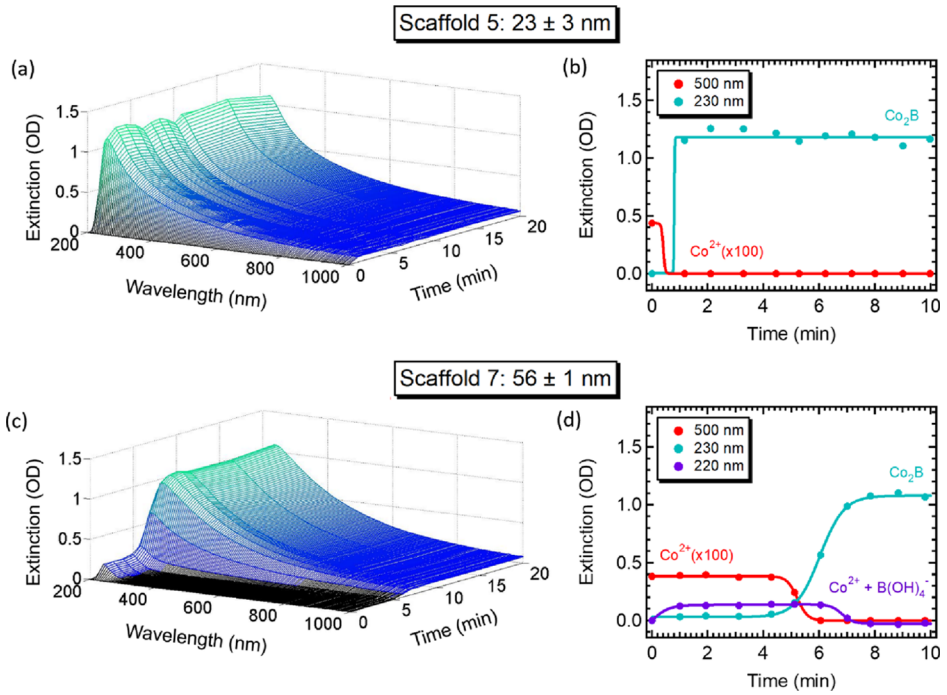

Figure 2. (a) Time-resolved extinction spectra for the formation of scaffold 5: 23 ± 3 nm Co_2B NPs over the course of 20 min. (b) Two wavelengths of interest are monitored for the first 10 min: 500 nm to highlight the disappearance of hydrated Co^{2+} ions and 230 nm to highlight the formation of Co_2B NPs. (c) Time-resolved extinction spectra for the formation of scaffold 7: 56 ± 1 nm Co_2B NPs over the course of 20 min. (d) Three wavelengths of interest are monitored for the first 10 min: 500 nm to highlight the disappearance of hydrated Co^{2+} ions, 230 nm to highlight the formation of Co_2B NPs, and 220 nm to highlight the interaction of Co^{2+} with $B(OH)_4^-$ in the presence of citrate. The 220 and 230 nm spectral contributions were deconvolved using SVD. For all spectra, the citrate contribution has been subtracted to better reveal the appearance of extinction below 300 nm.

tion spectra are displayed in Figure 2a,c for the first 20 min of scaffold formation. In these figures, the spectral contribution of citrate has been subtracted to better highlight the appearance of features below 300 nm.

The growth processes are visibly different with and without the addition of $B(OH)_4^-$. When no $B(OH)_4^-$ was added during nucleation, the extinction related to the Co_2B scaffold formed in less than 1 min and remained unchanged for the length of the observation (Figure 2a, scaffold 5: 23 ± 3 nm). No appreciable broadening of this signal occurred, suggesting that the reaction was complete within the first minute. When the same synthesis was performed with a $B(OH)_4^-/BH_4^-$ ratio of 1.00, the scaffold formation was significantly delayed (Figure 2c, scaffold 7: 56 ± 1 nm). Instead, almost immediately, a small absorption edge appeared at 220 nm and remained stable until minute 4. This edge then broadened and increased in intensity through minute 8 after which time the spectrum remained relatively unchanged for the remainder of the observation.

A similar intermediate 220 nm feature was previously reported in the formation of silver NPs and was hypothesized as arising from the association of borohydride with the surface of primary monomers.[56] However, in our system, the edge near 220 nm cannot be due to borohydride. Instead, it was identified as being related to an interaction between $B(OH)_4^-$ and hydrated Co^{2+} ions. In a separate experiment, when $B(OH)_4^-$ and Co^{2+} ions were combined in the presence of citrate, the hydrated Co^{2+} feature red-shifted from ∼500 to 520 nm and the UV absorption of $B(OH)_4^-$ also red-shifted, increasing the signal around 220 nm. These extinction spectra and further discussion are provided in Supporting Information Discussion S3. Importantly, the data suggest that a complex is formed between $B(OH)_4^-$ and Co^{2+} ions in the presence of citrate. The formation of this complex can be used to explain the growth process of larger Co_2B NPs.

To better understand the growth process and significance of the 220 nm signal, three wavelengths of interest are monitored over time in Figure 2b,d: 500 nm to probe the disappearance of hydrated Co^{2+} ions, 230 nm to probe the appearance of the Co_2B NP scaffold, and 220 nm to probe the proposed Co^{2+} + $B(OH)_4^-$ complex. The 220 and 230 nm spectral contributions were deconvolved with singular-value decomposition (SVD), as detailed in Supporting Information Discussion S3. In the case of scaffold 5, when no $B(OH)_4^-$ is present, Figure 2b confirms that the reaction between BH_4^- and $CoCl_2$ is rapid; hydrated Co^{2+} were no longer discernible in the spectrum within the first minute. In the case of scaffold 7, the presence of $B(OH)_4^-$ hindered BH_4^- from reacting with cobalt ions as quickly and the spectral contribution from hydrated Co^{2+} was still clearly visible until minute 6. When the Co_2B NP scaffold did begin to form, it did so at a slower rate, requiring almost 4 min for full growth. For both scaffolds, spectral contribution from the Co_2B NPs began to appear only when the cobalt ions began to be consumed, as would be expected. The SVD results also support the classification of the 220 nm edge as arising from the interaction between Co^{2+} and $B(OH)_4^-$ as its appearance is strongly correlated with the presence of hydrated Co^{2+} and its depletion with the appearance of the Co_2B scaffold.

In summary, the growth of Co_2B NP scaffolds may be promoted by the addition of $B(OH)_4^-$ alongside BH_4^-. Although $B(OH)_4^-$ is not a reducing agent, it does indeed affect the initial nucleation of cobalt ions, simply by slowing the process. When $B(OH)_4^-$ is present, a complex is formed with

DOI: 10.1021/acsami.8b00726
ACS Appl. Mater. Interfaces XXXX, XXX, XXX−XXX

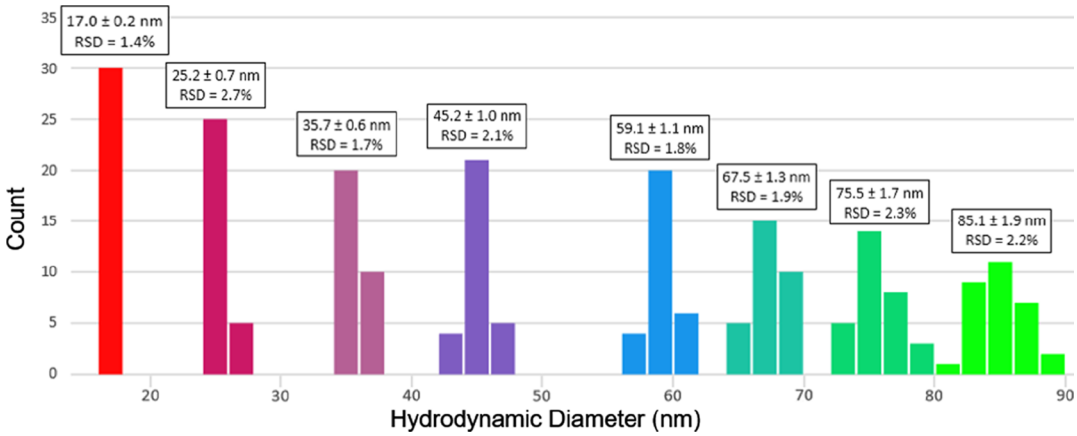

Figure 3. Fine control of Co_2B NP diameter over a large size range achieved with different $BH_4^-/B(OH)_4^-$ nucleation agent/growth agent ratios. Generally, smaller BH_4^-/Co^{2+} ratios and larger $B(OH)_4^-/BH_4^-$ ratios produce larger Co_2B diameters. Here, the $B(OH)_4^-/BH_4^-$ ratio ranges from 0 (red histogram) to 4 (neon green histogram) whereas the BH_4^-/Co^{2+} ratio ranges from 5 to 1, respectively. Average hydrodynamic diameter is reported with one standard deviation. RSD values are all under 3%, indicating a high monodispersity of resultant scaffolds.

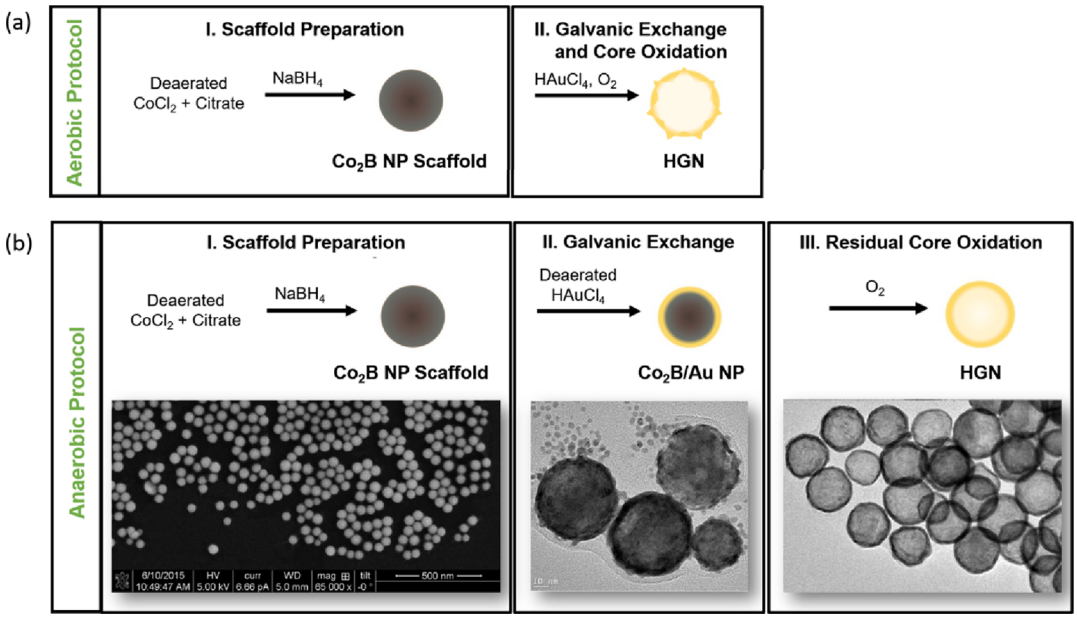

Figure 4. GE protocols for HGN synthesis. (a) Aerobic protocol: Co_2B NP scaffolds are prepared by wet-chemical reaction between cobalt ions and sodium borohydride, GE is carried out by the introduction of Co_2B NP scaffolds to aqueous gold ions, and the Co_2B NP core is simultaneously oxidized out of the shell by interaction with environmental oxygen. (b) Anaerobic protocol: GE and oxygenation steps are separated and the gold salt is deaerated so that GE may be carried out in the absence of environmental oxygen. A representative SEM image is provided for the Co_2B NPs formed in step I and representative HRTEM images are provided for the Co_2B NP/Au core/shell structures and resultant HGNs formed in steps II and III, respectively.

the hydrated cobalt ions, which hinders the BH_4^- from normal nucleation. In addition to slowing the initial reduction, $B(OH)_4^-$ aids particle growth, likely through the destabilization of primary clusters and promotion of coalescence processes. It has been well-established that BH_4^- serves as a stabilizing agent for NPs through electrostatic adsorption onto the particle surface.[47−49] If BH_4^- access is hindered, the stabilization of as-formed clusters could also be hindered. The less-stable clusters are more likely to aggregate and coalesce, resulting in the formation of larger particles. Although beyond the remit of this primarily synthetic investigation, further studies are needed to add insights into the Co_2B NP growth mechanism, particularly to separate growth by coalescence of the as-formed clusters from growth by additional reduction of ions in the electrical double layer.

Demonstrating Fine Control of Co_2B NP Diameter while Maintaining Monodispersity. We have shown that $B(OH)_4^-$ may be employed as a growth agent in the synthesis of Co_2B NPs. As demonstrated in Figure 3, high-quality Co_2B NPs with diameter ranging from ∼17 to 85 nm may be prepared with this method, all with RSD <3% and many with RSD <2%. In general, a greater $B(OH)_4^-/BH_4^-$ ratio results in larger Co_2B NP diameters. However, this trend is not without limit. There exists a threshold after which size can no longer be increased by increasing $B(OH)_4^-$ alone. At this point, larger sizes may be accessed by a reduction in BH_4^-. In this way, the size of the resultant Co_2B NPs represents a delicate interplay between the extent of nucleation and amount of growth agent. In Figure 3, the $B(OH)_4^-/BH_4^-$ ratio ranges from 0 (red

DOI: 10.1021/acsami.8b00726
ACS Appl. Mater. Interfaces XXXX, XXX, XXX−XXX

histogram) to 4 (neon green histogram), whereas the BH_4^-/Co^{2+} ratio ranges from 5 to 1, respectively.

Synthesis of HGNs: Galvanic Exchange and Controlled Oxidation of Co_2B NP Scaffolds. When using Co_2B NP scaffolds for the formation of HGNs, our findings reveal that the shell structure may be dictated not only by the starting scaffold (to control the overall size and shape) and the amount of metal provided for GE (to control the shell thickness) but also by the extent of competing oxidation reactions due to the presence of environmental oxygen. To demonstrate this, two protocols for HGN synthesis are illustrated in Figure 4. Both protocols involve the same steps: Co_2B NPs are prepared as previously described, GE is carried out between the Co_2B NP scaffold and chloroauric acid, and the residual Co_2B NP cores are oxidized into the solution by exposure to environmental oxygen to leave behind solvent-filled shells of gold. However, the protocols differ in the timing of oxygen introduction. In the aerobic protocol, GE and environmental oxygen exposure occur simultaneously. In the anaerobic protocol, these are separated into independent steps. In this way, a Co_2B/Au core/shell NP is allowed to form before the interaction of Co_2B with environmental oxygen. An SEM image is provided for the Co_2B NP scaffolds and an HRTEM image is provided for the Co_2B/Au core/shell NPs formed after GE as well as the HGNs formed after oxidation of the residual Co_2B cores.

To assess the effect of environmental oxygen on shell formation, scaffold 7 was taken through GE with 0.10−1.0 μmol $HAuCl_4$ using aerobic and anaerobic protocols. The optical and structural properties of the resultant HGNs were characterized with UV−vis and HRTEM, as shown in Figure 5. In Figure 5a, for each protocol, the wavelength of SPR maximum is plotted as a function of the amount of gold. As expected, regardless of protocol, when less gold was provided for GE, the SPR was red-shifted because of the formation of thinner shells. However, for given amounts of $HAuCl_4$, the anaerobic protocol consistently produced a redder SPR than the aerobic protocol. The extinction spectra of HGNs made with 0.30 μmol $HAuCl_4$ is provided as a representative example in Figure 5b. When oxygen was present during GE, the SPR was centered at 665 nm (dashed line). When GE was instead carried out in the absence of oxygen, the SPR was stronger and relatively red-shifted, centered at 760 nm (solid line). HRTEM reveals that these optical differences arise from structural ones. The aerobic shells are not continuous but resemble a patchwork collection of smaller gold particle domains (Figure 5c). The anaerobic shells, on the other hand, are smoother and more intact (Figure 5d). Extinction spectra and HRTEM images of HGNs made with the other amounts of $HAuCl_4$ are provided in Supporting Information Discussion S4.

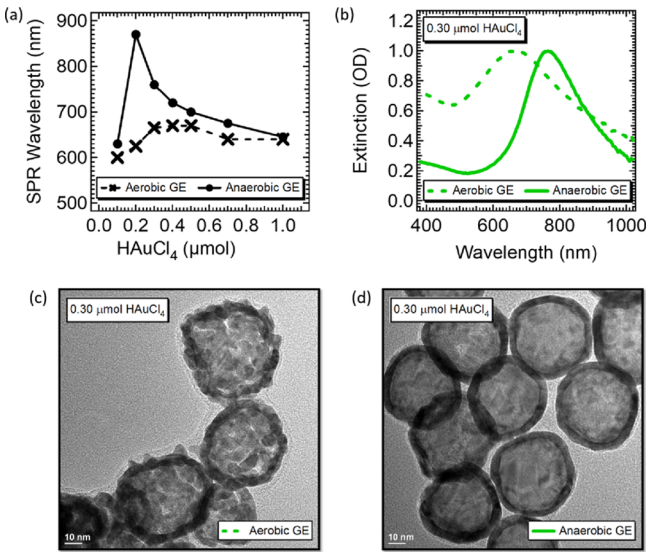

Figure 5. Optical and structural effects of oxygen during GE with scaffold 7. (a) SPR peak wavelengths of HGNs made via aerobic (dashed line) and anaerobic (solid line) GE protocols using 0.10−1.0 μmol $HAuCl_4$. (b) Example extinction spectra of HGNs made with 0.30 μmol $HAuCl_4$ using aerobic (dashed line) and anaerobic (solid line) protocols. (c,d) Corresponding HRTEM images; scale bar 10 nm.

Although the red shift between protocols was observed for the majority of the amounts of $HAuCl_4$ investigated, it is not without limits. The SPR values of HGNs for both protocols are in close agreement for the high and low amounts of $HAuCl_4$. This result can also be explained from a structural standpoint. At high volumes of gold, the anaerobic shell thickens and becomes more irregular, resembling the structure of the thick aerobic shell (e.g., the results for 1.0 μmol $HAuCl_4$ in Figures 5a, S5f). On the other hand, if the volume of gold is too low, the shell begins to resemble a cage structure, with missing portions of the shell wall. When the gold volume is lowered even further, there is not sufficient material for the shell to retain structural integrity once the residual Co_2B NP core is oxidized out. In this case, only large gold fragments remain and the SPR blue-shifts to ∼600 nm for both protocols (e.g., the results for 0.10 μmol $HAuCl_4$ in Figure 5a).

Importantly, the anaerobic GE protocol was able to produce and stabilize relatively thinner shells before they lost structural integrity. The degree to which the SPR red-shifted as the amount of $HAuCl_4$ was decreased is much greater for the anaerobic GE protocol overall. For instance, the anaerobic SPR shifted to 870 nm whereas the aerobic SPR was able to reach only 670 nm. We propose that because anaerobic GE allows the scaffold to be protected while it exchanges with gold, no competition exists between gold and oxygen during shell formation and gold is therefore able to reduce onto the scaffold in a more uniform manner. The uniformity of plating enables thinner shells to form and be continuous enough to remain intact. This is especially advantageous for tuning the SPR of small HGNs to longer wavelengths, which has been a difficult task as red-shifting a small particle requires the formation of a very thin shell. The red shift in SPR with anaerobic GE is demonstrated for the smaller diameter scaffold 5 in Supporting Information Discussion S4.

Finally, we also assessed the effect of oxygen during the final synthesis step of the anaerobic protocol, the residual Co_2B NP core oxidation. Specifically, we investigatedthe rate of Co_2B removal from the Co_2B NP/Au structures by varying the rate of oxygen addition. This work is discussed in Supporting Information Discussion S5, and the results suggest that the shell is still alterable even after GE. In effect, we show that a range of SPR frequencies, spanning upward of 100 nm, may be accessed from the same starting Co_2B NP scaffold and gold amount through different routes of oxygen introduction during steps I and II of synthesis. It is possible that larger shifts in SPR are obtainable with more finely controlled oxygenation during and after GE.

Demonstrating Twofold Tunability: Independent Control of HGN Diameter and SPR. With better synthetic

DOI: 10.1021/acsami.8b00726
ACS Appl. Mater. Interfaces XXXX, XXX, XXX−XXX

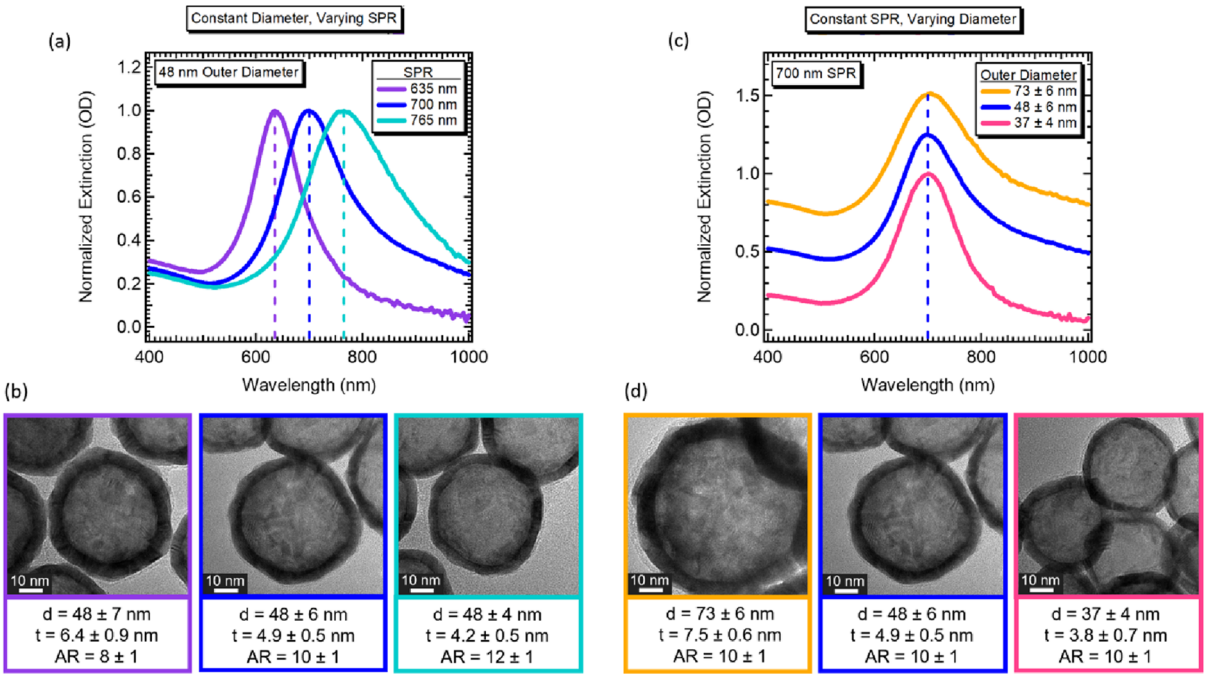

Figure 6. Demonstration of twofold tunability. (a) Normalized extinction for HGNs with the same outer diameter but different SPR: 48 nm HGNs with 635, 700, and 765 nm SPR. (b) Corresponding HRTEM images with average diameter (*d*), shell thickness (*t*), and aspect ratio (AR) as indicated; scale bar 10 nm. (c) Normalized extinction for HGNs with a different outer diameter but the same SPR: 73 ± 6, 48 ± 6, and 37 ± 4 nm HGNs with 700 nm SPR. After normalization, the 48 ± 6 and 73 ± 6 nm extinctions were offset on the y-axis by 0.25 and 0.50 OD, respectively. (d) Corresponding HRTEM images with *d*, *t*, and AR as indicated; scale bar 10 nm.

control of the Co_2B NP diameter and an understanding of how to achieve high-quality uniform shells, we demonstrate the twofold tunability of HGNs. As shown in Figure 6a, by controlling both diameter and shell thickness, we have synthesized HGNs of the same outer diameter with different SPRs. Conversely, as shown in Figure 6b, we have also synthesized HGNs of different outer diameters with the same SPR by keeping the aspect ratio constant. This degree of tunability is unique to date and is especially advantageous for HGN use in applications that are sensitive to both size and SPR. Furthermore, our approach provides opportunities to investigate the fundamental size dependence of photophysical and photocatalytic properties, such as those for plasmonic hot carriers, by enabling uniform energy distributions for a range of HGN sizes.

CONCLUSIONS

To control the HGN diameter, we have introduced an improved size control method for Co_2B NP scaffolds. By varying the relative amounts of BH_4^- nucleation and $B(OH)_4^-$ growth agents, high-quality Co_2B NPs were prepared with hydrodynamic diameters ranging from ∼17 to 85 nm and RSD <3%. To control HGN shell thickness and uniformity, oxygen must be regarded as a reactant in GE as it affects both the structural and optical properties. These findings provide important new insights into the mechanism of growth of HGNs with controlled SPRs and have broader implications for the growing field of conversion chemistry, particularly for the formation of hollow metal nanostructures through GE with cobalt or other air-sensitive materials. Finally, with this level of synthetic control, high-quality HGNs over a range of desired size and shell thickness combinations can be obtained, an achievement critical to many applications that require specific particle size or SPR wavelength.

ASSOCIATED CONTENT

Supporting Information

The Supporting Information is available free of charge on the ACS Publications website at DOI: 10.1021/acsami.8b00726.

Identity of the Co_2B NP scaffold, the hydrolysis of BH_4^- to $B(OH)_4^-$, the role of $B(OH)_4^-$ in Co_2B NP formation, SVD, and the effect of environmental oxygen during GE and residual core oxidation for the formation of HGNs from Co_2B NP scaffolds (PDF)

AUTHOR INFORMATION

Corresponding Author

*E-mail: zhang@ucsc.edu.

ORCID

Sarah A. Lindley: 0000-0002-6600-0412
Shaowei Chen: 0000-0002-3668-8551
Jin Z. Zhang: 0000-0003-3437-912X

Notes

The authors declare no competing financial interest.

ACKNOWLEDGMENTS

We are grateful to Delta Dental Health Associates, Smart Technologies, NASA through the Merced Nanomaterials Center for Energy and Sensing (MACES), and the W.M. Keck Center for Nanoscale Optofluidics QB3 Fellowship for funding. We acknowledge T. Yuzvinsky for SEM and the W.M. Keck Center for Nanoscale Optofluidics for use of the FEI Quanta 3D dual beam microscope. We acknowledge S. Gul and the Stanford Synchrotron Radiation Lightsource for XAS. We

also acknowledge J. Lee at UC Santa Cruz for NMR training and C. Song at the Molecular Foundry NCEM for HRTEM training. Work at the Molecular Foundry was supported by the Office of Science, Office of Basic Energy Sciences, of the U.S. Department of Energy under contract no. DE-AC02-05CH11231. We also acknowledge the contribution from the Joint Center for Artificial Photosynthesis, a DOE Energy Innovation Hub, supported through the Office of Science of the U.S. Department of Energy under award no. DE-SC0004993. S.A.L. acknowledges D. Wheeler for training and fruitful discussions as well as M. Martos and M. Tran for aid in synthesis.

REFERENCES

(1) Papavassiliou, G. C. Optical Properties of Small Inorganic and Organic Metal Particles. *Prog. Solid State Chem. Res.* **1979**, *12*, 185−271.

(2) Creighton, J. A.; Eadon, D. G. Ultraviolet-Visible Absorption Spectra of the Colloidal Metallic Elements. *J. Chem. Soc., Faraday Trans.* **1991**, *87*, 3881−3891.

(3) Link, S.; El-Sayed, M. A. Size and Temperature Dependence of the Plasmon Absorption of Colloidal Gold Nanoparticles. *J. Phys. Chem. B* **1999**, *103*, 4212−4217.

(4) Sherry, L. J.; Jin, R.; Mirkin, C. A.; Schatz, G. C.; Van Duyne, R. P. Localized Surface Plasmon Resonance Spectroscopy of Single Silver Triangular Nanoprisms. *Nano Lett.* **2006**, *6*, 2060−2065.

(5) Jain, P. K.; Lee, K. S.; El-Sayed, I. H.; El-Sayed, M. A. Calculated Absorption and Scattering Properties of Gold Nanoparticles of Different Size, Shape, and Composition: Applications in Biological Imaging and Biomedicine. *J. Phys. Chem. B* **2006**, *110*, 7238−7248.

(6) Lim, W. Q.; Gao, Z. Plasmonic Nanoparticles in Biomedicine. *Nano Today* **2016**, *11*, 168−188.

(7) Lane, L. A.; Qian, X.; Nie, S. SERS Nanoparticles in Medicine: From Label-Free Detection to Spectroscopic Tagging. *Chem. Rev.* **2015**, *115*, 10489−10529.

(8) Peng, H.-I.; Strohsahl, C. M.; Leach, K. E.; Krauss, T. D.; Miller, B. L. Label-Free DNA Detection on Nanostructured Ag Surfaces. *ACS Nano* **2009**, *3*, 2265−2273.

(9) Kosaka, P. M.; Pini, V.; Ruz, J. J.; da Silva, R. A.; González, M. U.; Ramos, D.; Calleja, M.; Tamayo, J. Detection of Cancer Biomarkers in Serum Using a Hybrid Mechanical and Optoplasmonic Nanosensor. *Nat. Nanotechnol.* **2014**, *9*, 1047−1053.

(10) You, J.; Zhang, G.; Li, C. Exceptionally High Payload of Doxorubicin in Hollow Gold Nanospheres for Near-Infrared Light-Triggered Drug Release. *ACS Nano* **2010**, *4*, 1033−1041.

(11) Vijayaraghavan, P.; Liu, C.-H.; Vankayala, R.; Chiang, C.-S.; Hwang, K. C. Designing Multi-Branched Gold Nanoechinus for NIR Light Activated Dual Modal Photodynamic and Photothermal Therapy in the Second Biological Window. *Adv. Mater.* **2014**, *26*, 6689−6695.

(12) Xing, R.; Liu, K.; Jiao, T.; Zhang, N.; Ma, K.; Zhang, R.; Zou, Q.; Ma, G.; Yan, X. An Injectable Self-Assembling Collagen-Gold Hybrid Hydrogel for Combinatorial Antitumor Photothermal/Photodynamic Therapy. *Adv. Mater.* **2016**, *28*, 3669−3676.

(13) Yang, P.; Zheng, J.; Xu, Y.; Zhang, Q.; Jiang, L. Colloidal Synthesis and Applications of Plasmonic Metal Nanoparticles. *Adv. Mater.* **2016**, *28*, 10508−10517.

(14) Maier, S. A.; Brongersma, M. L.; Kik, P. G.; Meltzer, S.; Requicha, A. A. G.; Atwater, H. A. Plasmonics—A Route to Nanoscale Optical Devices. *Adv. Mater.* **2001**, *13*, 1501−1505.

(15) Sheldon, M. T.; Van de Groep, J.; Brown, A. M.; Polman, A.; Atwater, H. A. Plasmoelectric Potentials in Metal Nanostructures. *Science* **2014**, *346*, 828−831.

(16) Choi, H.; Ko, S.-J.; Choi, Y.; Joo, P.; Kim, T.; Lee, B. R.; Jung, J.-W.; Choi, H. J.; Cha, M.; Jeong, J.-R.; Hwang, I.-W.; Song, M. H.; Kim, B.-S.; Kim, J. Y. Versatile Surface Plasmon Resonance of Carbon-Dot Supported Silver Nanoparticles in Polymer Optoelectronic Devices. *Nat. Photonics* **2013**, *7*, 732−738.

(17) Kim, T.; Kang, H.; Jeong, S.; Kang, D. J.; Lee, C.; Lee, C.-H.; Seo, M.-K.; Lee, J.-Y.; Kim, B. J. Au@Polymer Core-Shell Nanoparticles for Simultaneously Enhancing Efficiency and Ambient Stability of Organic Optoelectronic Devices. *ACS Appl. Mater. Interfaces* **2014**, *6*, 16956−16965.

(18) Zhong, L.; Jiang, Y.; Liow, C.; Meng, F.; Sun, Y.; Chandran, B. K.; Liang, Z.; Jiang, L.; Li, S.; Chen, X. Highly Sensitive Electro-Plasmonic Switches Based on Fivefold Stellate Polyhedral Gold Nanoparticles. *Small* **2015**, *11*, 5395−5401.

(19) Talley, C. E.; Jackson, J. B.; Oubre, C.; Grady, N. K.; Hollars, C. W.; Lane, S. M.; Huser, T. R.; Nordlander, P.; Halas, N. J. Surface-Enhanced Raman Scattering from Individual Au Nanoparticles and Nanoparticle Dimer Substrates. *Nano Lett.* **2005**, *5*, 1569−1574.

(20) Linic, S.; Christopher, P.; Ingram, D. B. Plasmonic-Metal Nanostructures for Efficient Conversion of Solar to Chemical Energy. *Nat. Mater.* **2011**, *10*, 911−921.

(21) Clavero, C. Plasmon-Induced Hot-Electron Generation at Nanoparticle/Metal-Oxide Interfaces for Photovoltaic and Photocatalytic Devices. *Nat. Photonics* **2014**, *8*, 95−103.

(22) Meng, X.; Liu, L.; Ouyang, S.; Xu, H.; Wang, D.; Zhao, N.; Ye, J. Nanometals for Solar-to-Chemical Energy Conversion: From Semiconductor-Based Photocatalysis to Plasmon-Mediated Photocatalysis and Photo-Thermocatalysis. *Adv. Mater.* **2016**, *28*, 6781−6803.

(23) Christopher, P.; Xin, H.; Linic, S. Visible-Light-Enhanced Catalytic Oxidation Reactions on Plasmonic Silver Nanostructures. *Nat. Chem.* **2011**, *3*, 467−472.

(24) Liu, H.; Meng, X.; Dao, T. D.; Zhang, H.; Li, P.; Chang, K.; Wang, T.; Li, M.; Nagao, T.; Ye, J. Conversion of Carbon Dioxide by Methane Reforming under Visible-Light Irradiation: Surface-Plasmon-Mediated Nonpolar Molecule Activation. *Angew. Chem., Int. Ed.* **2015**, *54*, 11545−11549.

(25) Sun, Y.; Mayers, B.; Xia, Y. Metal Nanostructures with Hollow Interiors. *Adv. Mater.* **2003**, *15*, 641−646.

(26) Mahmoud, M. A.; Snyder, B.; El-Sayed, M. A. Surface Plasmon Fields and Coupling in the Hollow Gold Nanoparticles and Surface-Enhanced Raman Spectroscopy. Theory and Experiment. *J. Phys. Chem. C* **2010**, *114*, 7436−7443.

(27) Zeng, J.; Zhang, Q.; Chen, J.; Xia, Y. A Comparison Study of the Catalytic Properties of Au-Based Nanocages, Nanoboxes, and Nanoparticles. *Nano Lett.* **2010**, *10*, 30−35.

(28) Genç, A.; Patarroyo, J.; Sancho-Parramon, J.; Bastús, N. G.; Puntes, V.; Arbiol, J. Hollow Metal Nanostructures for Enhanced Plasmonics: Synthesis, Local Plasmonic Properties, and Applications. *Nanophotonics* **2017**, *6*, 193−213.

(29) Hazra, B.; Chandra, M. Plasmon Hybridization Mediated Structure-Specific Refractive Index Sensitivity of Hollow Gold Nanoprism in the Vis-NIR Region. *ACS Sens.* **2016**, *1*, 536−542.

(30) Lu, B.; Liu, A.; Wu, H.; Shen, Q.; Zhao, T.; Wang, J. Hollow Au−Cu2O Core−Shell Nanoparticles with Geometry-Dependent Optical Properties as Efficient Plasmonic Photocatalysts under Visible Light. *Langmuir* **2016**, *32*, 3085−3094.

(31) Schwartzberg, A. M.; Olson, T. Y.; Talley, C. E.; Zhang, J. Z. Synthesis, Characterization, and Tunable Optical Properties of Hollow Gold Nanospheres. *J. Phys. Chem. B* **2006**, *110*, 19935−19944.

(32) Newhouse, R. J.; Wang, H.; Hensel, J. K.; Wheeler, D. A.; Zou, S.; Zhang, J. Z. Coherent Vibrational Oscillations of Hollow Gold Nanospheres. *J. Phys. Chem. Lett.* **2011**, *2*, 228−235.

(33) Dowgiallo, A.-M.; Schwartzberg, A. M.; Knappenberger, K. L. Structure-Dependent Coherent Acoustic Vibrations of Hollow Gold Nanospheres. *Nano Lett.* **2011**, *11*, 3258−3262.

(34) Dowgiallo, A.-M.; Knappenberger, K. L. Ultrafast Electron-Phonon Coupling in Hollow Gold Nanospheres. *Phys. Chem. Chem. Phys.* **2011**, *13*, 21585−21592.

(35) Chandra, M.; Dowgiallo, A.-M.; Knappenberger, K. L. Controlled Plasmon Resonance Properties of Hollow Gold Nanosphere Aggregates. *J. Am. Chem. Soc.* **2010**, *132*, 15782−15789.

(36) Preciado-Flores, S.; Wang, D.; Wheeler, D. A.; Newhouse, R.; Hensel, J. K.; Schwartzberg, A.; Wang, L.; Zhu, J.; Barboza-Flores, M.; Zhang, J. Z. Highly Reproducible Synthesis of Hollow Gold

DOI: 10.1021/acsami.8b00726
ACS Appl. Mater. Interfaces XXXX, XXX, XXX−XXX

Nanospheres with Near Infrared Surface Plasmon Absorption Using PVP as a Stabilizing Agent. *J. Mater. Chem.* **2011**, *21*, 2344−2350.
(37) Adams, S.; Thai, D.; Mascona, X.; Schwartzberg, A. M.; Zhang, J. Z. Key Factors Affecting the Reproducibility of Synthesis and Growth Mechanism of Near-Infrared Absorbing Hollow Gold Nanospheres. *Chem. Mater.* **2014**, *26*, 6805−6810.
(38) Adams, S.; Zhang, J. Z. Unique Optical Properties and Applications of Hollow Gold Nanospheres (HGNs). *Coord. Chem. Rev.* **2016**, *320*−*321*, 18−37.
(39) Schwartzberg, A. M.; Oshiro, T. Y.; Zhang, J. Z.; Huser, T.; Talley, C. E. Improving Nanoprobes Using Surface-Enhanced Raman Scattering from 30-nm Hollow Gold Particles. *Anal. Chem.* **2006**, *78*, 4732−4736.
(40) Lee, S.; Chon, H.; Lee, M.; Choo, J.; Shin, S. Y.; Lee, Y. H.; Rhyu, I. J.; Son, S. W.; Oh, C. H. Surface-Enhanced Raman Scattering Imaging of HER2 Cancer Markers Overexpressed in Single MCF7 Cells Using Antibody Conjugated Hollow Gold Nanospheres. *Biosens. Bioelectron.* **2009**, *24*, 2260−2263.
(41) Lu, W.; Melancon, M. P.; Xiong, C.; Huang, Q.; Elliott, A.; Song, S.; Zhang, R.; Flores, L. G.; Gelovani, J. G.; Wang, L. V.; Ku, G.; Stafford, R. J.; Li, C. Effects of Photoacoustic Imaging and Photothermal Ablation Therapy Mediated by Targeted Hollow Gold Nanospheres in an Orthotopic Mouse Xenograft Model of Glioma. *Cancer Res.* **2011**, *71*, 6116−6121.
(42) Liang, H.-P.; Wan, L.-J.; Bai, C.-L.; Jiang, L. Gold Hollow Nanospheres: Tunable Surface Plasmon Resonance Controlled by Interior-Cavity Sizes. *J. Phys. Chem. B* **2005**, *109*, 7795−7800.
(43) Chen, Y.; Liew, K. Y.; Li, J. Size Controlled Synthesis of Co Nanoparticles by Combination of Organic Solvent and Surfactant. *Appl. Surf. Sci.* **2009**, *255*, 4039−4044.
(44) Dávila-Ibáñez, A. B.; Legido-Soto, J. L.; Rivas, J.; Salgueirino, V. Amorphous Tunable-Size Co-B Magnetic Nanoparticles from the Cobalt-Catalyzed NaBH4 Hydrolysis. *Phys. Chem. Chem. Phys.* **2011**, *13*, 20146−20154.
(45) Pu, Y.-C.; Song, F.; Zhang, W.; Lindley, S.; Adams, S.; Zhang, J. Z. Size-Tunable Synthesis of Hollow Gold Nanospheres through Control of Reaction Temperature. *Part. Part. Syst. Charact.* **2017**, *34*, 1600255.
(46) An, K.; Hyeon, T. Synthesis and Biomedical Applications of Hollow Nanostructures. *Nano Today* **2009**, *4*, 359−373.
(47) Chen, M.; Gao, L. Synthesis and Characterization of Ag Nanoshells by a Facile Sacrificial Template Route through in situ Replacement Reaction. *Inorg. Chem.* **2006**, *45*, 5145−5149.
(48) Zeng, J.; Huang, J.; Lu, W.; Wang, X.; Wang, B.; Zhang, S.; Hou, J. Necklace-like Noble-Metal Hollow Nanoparticle Chains: Synthesis and Tunable Optical Properties. *Adv. Mater.* **2007**, *19*, 2172−2176.
(49) Liang, H.-P.; Zhang, H.-M.; Hu, J.-S.; Guo, Y.-G.; Wan, L.-J.; Bai, C.-L. Pt Hollow Nanospheres: Facile Synthesis and Enhanced Electrocatalysis. *Angew. Chem.* **2004**, *116*, 1566−1569.
(50) Glavee, G. N.; Klabunde, K. J.; Sorensen, C. M.; Hadjapanayis, G. C. Borohydride Reductions of Metal Ions. A New Understanding of the Chemistry Leading to Nanoscale Particles of Metals, Borides, and Metal Borates. *Langmuir* **1992**, *8*, 771−773.
(51) Glavee, G. N.; Klabunde, K. J.; Sorensen, C. M.; Hadjipanayis, G. C. Borohydride Reduction of Cobalt Ions in Water. Chemistry Leading to Nanoscale Metal, Boride, or Borate Particles. *Langmuir* **1993**, *9*, 162−169.
(52) Masa, J.; Weide, P.; Peeters, D.; Sinev, I.; Xia, W.; Sun, Z.; Somsen, C.; Muhler, M.; Schuhmann, W. Amorphous Cobalt Boride (Co_2B) as a Highly Efficient Nonprecious Catalyst for Electrochemical Water Splitting: Oxygen and Hydrogen Evolution. *Adv. Energy Mater.* **2016**, *6*, 1502313.
(53) LaMer, V. K.; Dinegar, R. H. Theory, Production and Mechanism of Formation of Monodispersed Hydrosols. *J. Am. Chem. Soc.* **1950**, *72*, 4847−4854.
(54) Thanh, N. T. K.; Maclean, N.; Mahiddine, S. Mechanisms of Nucleation and Growth of Nanoparticles in Solution. *Chem. Rev.* **2014**, *114*, 7610−7630.
(55) Bartecki, A.; Tłaczała, T. The Color of Transition Metal Compounds. I.Trichromaticity Colorimetry of Aqueous Solutions of Some Cr(III), Co(II), Ni(II) and Cu(II) Compounds. *Spectrosc. Lett.* **1990**, *23*, 727−739.
(56) Van Hyning, D. L.; Zukoski, C. F. Formation Mechanisms and Aggregation Behavior of Borohydride Reduced Silver Particles. *Langmuir* **1998**, *14*, 7034−7046.
(57) Van Hyning, D. L.; Klemperer, W. G.; Zukoski, C. F. Characterization of Colloidal Stability during Precipitation Reactions. *Langmuir* **2001**, *17*, 3120−3127.
(58) Van Hyning, D. L.; Klemperer, W. G.; Zukoski, C. F. Silver Nanoparticle Formation: Predictions and Verification of the Aggregative Growth Model. *Langmuir* **2001**, *17*, 3128−3135.
(59) Richards, V. N.; Rath, N. P.; Buhro, W. E. Pathway from a Molecular Precursor to Silver Nanoparticles: The Prominent Role of Aggregative Growth. *Chem. Mater.* **2010**, *22*, 3556−3567.
(60) Polte, J.; Erler, R.; Thünemann, A. F.; Sokolov, S.; Ahner, T. T.; Rademann, K.; Emmerling, F.; Kraehnert, R. Nucleation and Growth of Gold Nanoparticles Studied via In Situ Small Angle X-Ray Scattering at Millisecond Time Resolution. *ACS Nano* **2010**, *4*, 1076−1082.
(61) Polte, J.; Tuaev, X.; Wuithschick, M.; Fischer, A.; Thuenemann, A. F.; Rademann, K.; Kraehnert, R.; Emmerling, F. Formation Mechanism of Colloidal Silver Nanoparticles: Analogies and Differences to the Growth of Gold Nanoparticles. *ACS Nano* **2012**, *6*, 5791−5802.
(62) Wuithschick, M.; Paul, B.; Bienert, R.; Sarfraz, A.; Vainio, U.; Sztucki, M.; Kraehnert, R.; Strasser, P.; Rademann, K.; Emmerling, F.; Polte, J. Size-Controlled Synthesis of Colloidal Silver Nanoparticles Based on Mechanistic Understanding. *Chem. Mater.* **2013**, *25*, 4679−4689.
(63) Netskina, O. V.; Komova, O. V.; Simagina, V. I.; Odegova, G. V.; Prosvirin, I. P.; Bulavchenko, O. A. Aqueous-Alkaline NaBH4 solution: The Influence of Storage Duration of Solutions on Reduction and Activity of Cobalt Catalysts. *Renewable Energy* **2016**, *99*, 1073−1081.

DOI: 10.1021/acsami.8b00726
ACS Appl. Mater. Interfaces XXXX, XXX, XXX−XXX